LETTER

doi:10.1038/nature23019

Synaptic organization of visual space in primary visual cortex

M. Florencia Iacaruso[1]†*, Ioana T. Gasler[1]* & Sonja B. Hofer[1]

How a sensory stimulus is processed and perceived depends on the surrounding sensory scene. In the visual cortex, contextual signals can be conveyed by an extensive network of intra- and inter-areal excitatory connections that link neurons representing stimulus features separated in visual space[1–4]. However, the connectional logic of visual contextual inputs remains unknown; it is not clear what information individual neurons receive from different parts of the visual field, nor how this input relates to the visual features that a neuron encodes, defined by its spatial receptive field. Here we determine the organization of excitatory synaptic inputs responding to different locations in the visual scene by mapping spatial receptive fields in dendritic spines of mouse visual cortex neurons using two-photon calcium imaging. We find that neurons receive functionally diverse inputs from extended regions of visual space. Inputs representing similar visual features from the same location in visual space are more likely to cluster on neighbouring spines. Inputs from visual field regions beyond the receptive field of the postsynaptic neuron often synapse on higher-order dendritic branches. These putative long-range inputs are more frequent and more likely to share the preference for oriented edges with the postsynaptic neuron when the receptive field of the input is spatially displaced along the axis of the receptive field orientation of the postsynaptic neuron. Therefore, the connectivity between neurons with displaced receptive fields obeys a specific rule, whereby they connect preferentially when their receptive fields are co-oriented and co-axially aligned. This organization of synaptic connectivity is ideally suited for the amplification of elongated edges, which are enriched in the visual environment, and thus provides a potential substrate for contour integration and object grouping.

Understanding the mechanisms of sensory processing requires uncovering the precise relationship between synaptic connectivity and function of neurons in cortical circuits. Local connectivity between neurons follows certain rules. For example, neighbouring layer (L)2/3 pyramidal neurons in rodent visual cortex preferentially connect if they receive common synaptic input[5,6] or if they respond to similar stimulus features within their receptive fields (RFs)[7–10]. However, the rules of long-range synaptic connectivity remain poorly understood. A substantial fraction of the synaptic inputs a cortical neuron receives originate outside its local network[11] and, in sensory cortices, many inputs stem from neurons representing distant topographic positions[1,2]. Long-range lateral projections in cat and primate primary visual cortex (V1) preferentially (but not exclusively) link orientation columns with similar preferences[2,12–14], and in some species these extend along the axis of the retinotopic map that corresponds to their preferred stimulus orientation[13,15,16]. While these studies reveal a degree of functional specificity of long-range projections, at least in animals with cortical columns, it is still unclear what repertoire of visual information a single neuron receives from the extended visual scene, and how this visual input relates to a neuron's preference for particular visual features. This knowledge is important for uncovering the circuit mechanisms of contextual processing and related perceptual Gestalt phenomena, such as integration of contours and object grouping in the visual environment[17,18].

To determine the visual response properties of synaptic inputs onto neurons in mouse primary visual cortex (V1) we used two-photon imaging of calcium signals in dendritic spines[19–21] on L2/3 pyramidal cells sparsely expressing the genetically encoded calcium indicator GCaMP6s[20] (Fig. 1a). Using sparse noise stimuli, we mapped the structure of spatial RFs on the basis of calcium signals observed in individual dendritic spines and nearby dendritic stretches (Fig. 1b–e). We isolated synaptic responses of individual spines by removing the contribution of the dendritic calcium signal from the spine calcium signal using robust regression[20,21] (Extended Data Fig. 1; see Methods and Extended Data Fig. 9 for controls). We found that 49% of spines were visually responsive ($n = 1{,}017$ of 2,072 spines, 21 mice), and 69% of those exhibited significant spatial RFs (Fig. 1e; RF size $= 211 \pm 78$ square degrees, mean $\pm$ s.d.). The spatial RF describes the relative position of ON (response to light increments) and OFF (response to light decrements) subfields in visual space, and provides information about visual features to which a neuron is most sensitive, including their orientation, phase, spatial frequency, location and size.

We first asked how spines with different visual feature preferences were distributed along the dendrite and if neighbouring spines shared preferences for visual features. As a measure of RF similarity, we computed a pixel-by-pixel correlation coefficient between pairs of RF maps[8]. On average, spatial RF correlations were weakly positive (0.1 ± 0.2, mean $\pm$ s.d.), but RF shapes and positions were very diverse, and only a small fraction of inputs shared highly similar RF maps (Figs 1f, 4.4% spine pairs with spatial RF correlation >0.5). Notably, nearby spines were more likely to have correlated RF maps than spines further apart (Fig. 1g, $P = 0.002$). Consistent with previous results[20], this clustering did not depend on similarity of orientation preference (Fig. 1h, $P = 0.7$), as determined from the apposition angle of ON and OFF subfields of each RF (Extended Data Fig. 2; see Methods), but instead on the co-localization of RF subfields in visual space (Extended Data Fig. 3). Therefore, synaptic inputs tend to cluster over short dendritic distances if they respond to similar visual features that occupy similar regions in visual space, consistent with observations that neighbouring inputs are more frequently co-active[22].

To compare response properties of synaptic inputs with those of the postsynaptic cell, we also mapped the spatial RFs of dendrites on which the spines resided (Figs 1d and 2a). Dendritic calcium signals extended across entire branches within the imaged region (correlation coefficient between dendritic segments $= 0.91 \pm 0.08$), and RFs derived from dendritic activity closely resembled those derived from calcium signals in the cell body (Extended Data Fig. 4). Under our experimental conditions, most dendritic signals thus probably arose from action potentials back-propagating from the soma or were generated in the

[1]Biozentrum, University of Basel, Klingelbergstrasse 50/70, CH-4056 Basel, Switzerland. †Present address: Department of Physiology, Anatomy and Genetics, University of Oxford, Oxford OX1 3PT, UK.
*These authors contributed equally to this work.

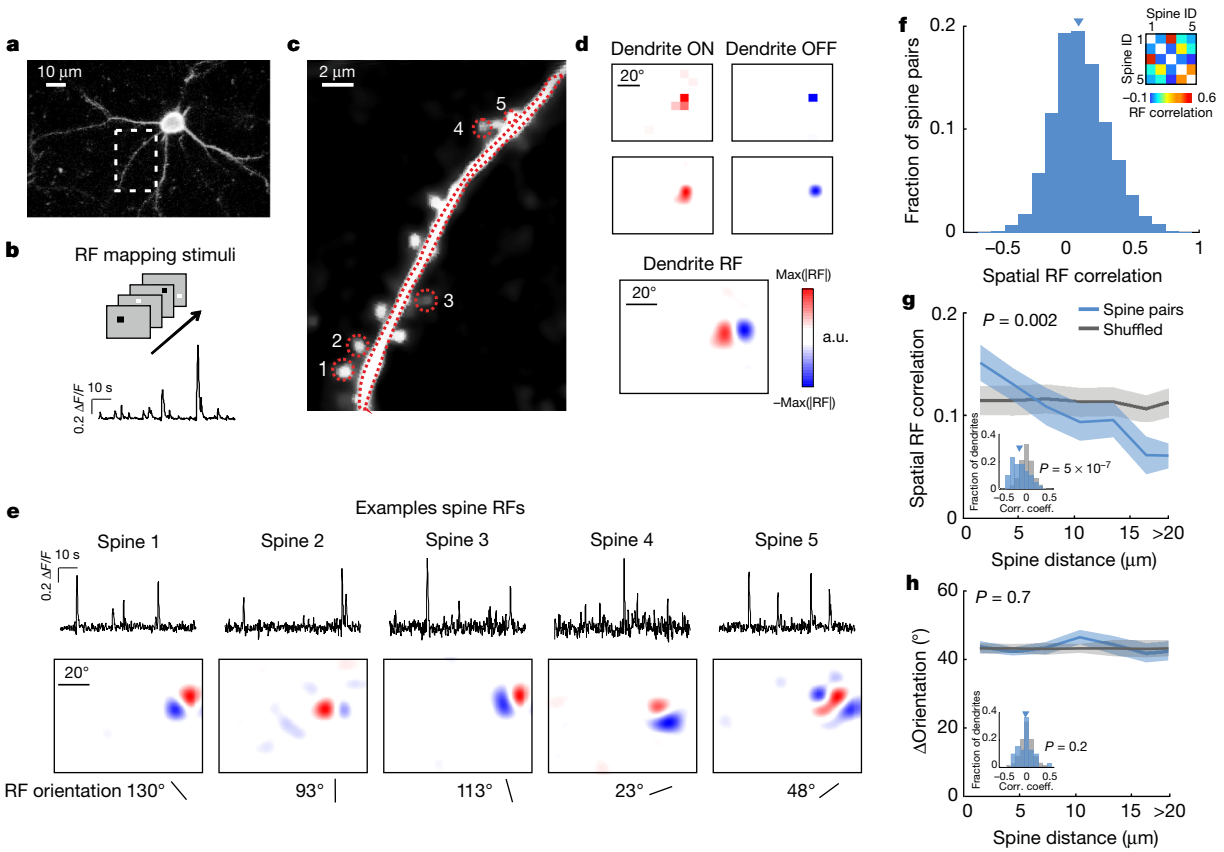

Figure 1 | Dendritic clustering of synaptic inputs with similar receptive fields. a, *Z*-projection of a layer 2/3 neuron expressing GCaMP6s in mouse V1. **b**, Schematic of receptive field (RF) mapping stimuli and a representative calcium fluorescence trace of the dendrite in **c**. **c**, Dendritic segment indicated in **a**. **d**, Raw (top), smoothed (middle) and combined (bottom) ON and OFF RF subfield maps from calcium signals extracted from the ROI over the dendrite shown in **c**. a.u., arbitrary units. Colour intensity denotes response strength to light increments (ON, red) and light decrements (OFF, blue). **e**, Spine calcium signals after removal of the dendritic component (top row), smoothed RFs (middle row), and orientation preference derived from the RFs (bottom row) of the example spines in **c**. **f**, The distribution of pairwise spatial RF correlation coefficients for all imaged spine pairs ($n = 3{,}966$ spine pairs, 74 dendrites, 21 mice). Triangle indicates median. Inset, example matrix of correlation coefficients of RFs from the spines in **e**. **g**, **h**, Relationship between the dendritic distance separating pairs of spines and their spatial RF correlation coefficients (**g**) and between spine-pair distances and the difference in their orientation preference (**h**, ΔOrientation). Shading represent s.e.m. *P* values from permutation test. Inset, the distribution of correlation coefficients between spine-pair distance and spatial RF correlation (**g**), or difference in orientation preference (**h**) for individual dendrites. *P* values from Wilcoxon signed-rank test, $n = 3{,}728$ spine pairs, 39 dendrites, 18 mice.

dendrite but induced somatic action potentials[23,24]. Therefore, we used global dendritic signals as a proxy for the output activity of the postsynaptic neuron. Computing the distance in visual space between RF centres of the postsynaptic neuron and its spines allowed us to determine the distribution of inputs from different parts of the visual field (Fig. 2a). Although the majority of inputs overlapped retinotopically (43% spines, 243 of 563, spine–dendrite RF centre distance <15°), the RFs of 28% of spines (159 of 563) were separated by more than 30° from the neuron's RF and therefore provided visual information from positions outside of the neuron's classical RF (Fig. 2a, b). The majority of synaptic inputs with displaced RFs probably originate from neurons >200 µm apart (Extended Data Fig. 5) or from sources outside of V1. These retinotopically displaced visual inputs were more numerous on more superficial neurons and dendrites, and on higher-order dendrites further away from the cell body (Fig. 2c, d and Extended Data Fig. 6). We found a coarse retinotopic organization of visual inputs across the dendritic tree with a significant gradient in visual space elevation relative to the postsynaptic cell's RF, consistent with the direction of retinotopic gradients in mouse V1 (Extended Data Fig. 7).

We next determined the relationship between the visual feature preferences of synaptic inputs and the postsynaptic neuron, and examined how this relationship changes as a function of RF separation. Of synaptic inputs whose RFs largely overlapped with that of the postsynaptic neuron (RF centre distance <15°), many preferred orientations similar to that of the postsynaptic neuron, while fewer inputs preferred orthogonal orientations (Fig. 2e, $P < 0.0001$, permutation test). These results are consistent with previous studies showing functionally specific connectivity in local networks in visual cortex[7–10].

By contrast, little is known about the functional properties of synaptic inputs originating from cells that process visual information remote from the RF of the postsynaptic neuron, even though these constitute a substantial fraction of inputs onto cortical neurons. We found that synaptic inputs with RFs displaced by more than 30° from the RF of the postsynaptic cell also showed functional specificity, with the majority of inputs preferring orientations similar to the postsynaptic neuron (Fig. 2f, $P = 0.02$). Notably, however, this organization of connectivity strongly depended on the position of the input RFs relative to the RF of the postsynaptic cell (Fig. 3). Specifically, the relationship between orientation preference and connectivity was only apparent for inputs with RFs displaced in visual space along or close to the axis of the postsynaptic neuron's RF orientation ('co-axial visual space', $P = 0.001$; Fig. 3a, b, d). By contrast, retinotopically displaced inputs from the axis orthogonal to the postsynaptic neuron's RF orientation were less numerous ('orthogonal visual space', 39%, 62 of 159 visually displaced RFs), and they were not biased towards sharing the

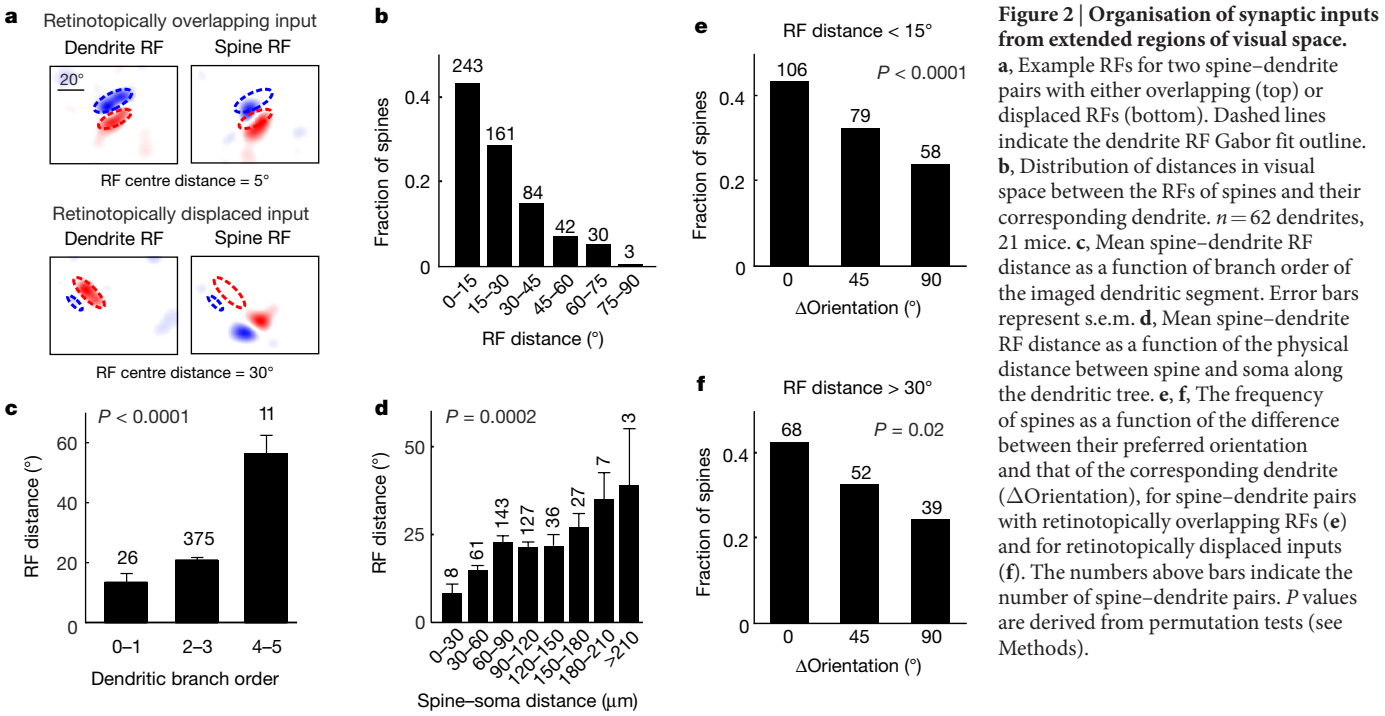

Figure 2 | Organisation of synaptic inputs from extended regions of visual space. **a**, Example RFs for two spine–dendrite pairs with either overlapping (top) or displaced RFs (bottom). Dashed lines indicate the dendrite RF Gabor fit outline. **b**, Distribution of distances in visual space between the RFs of spines and their corresponding dendrite. $n = 62$ dendrites, 21 mice. **c**, Mean spine–dendrite RF distance as a function of branch order of the imaged dendritic segment. Error bars represent s.e.m. **d**, Mean spine–dendrite RF distance as a function of the physical distance between spine and soma along the dendritic tree. **e**, **f**, The frequency of spines as a function of the difference between their preferred orientation and that of the corresponding dendrite (ΔOrientation), for spine–dendrite pairs with retinotopically overlapping RFs (**e**) and for retinotopically displaced inputs (**f**). The numbers above bars indicate the number of spine–dendrite pairs. *P* values are derived from permutation tests (see Methods).

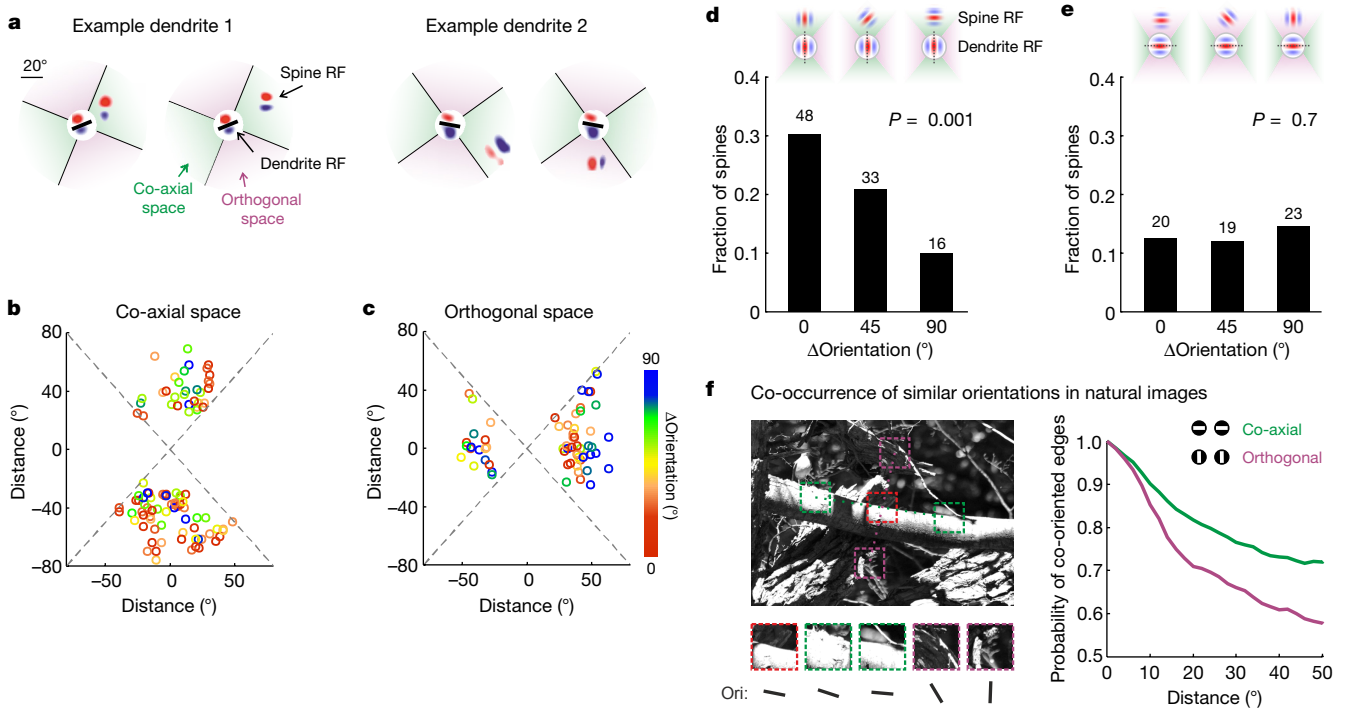

Figure 3 | Preferential synaptic input from neurons with co-oriented and co-axially aligned receptive fields. **a**, Two example dendrite RFs with two retinotopically displaced spine RFs each. The visual field was divided into two sectors relative to the orientation of the dendrite RF: the co-axial visual space refers to the region around the orientation axis of the RF (between −45° and +45°) running through its centre, the orthogonal region occupies the remainder of visual space. **b**, **c**, Position in visual space and orientation difference relative to the dendrite RF of spines with displaced RFs located in co-axial (**b**, 97 spines) or orthogonal (**c**, 62 spines) visual space. Circles indicate individual spines. Colour denotes the difference in orientation preference (ΔOrientation) between the spine and dendrite. **d**, **e**, The frequency of spines with displaced RFs as a function of the difference in their preferred orientation from that of the corresponding dendrite for spines with RFs located in co-axial (**d**) or orthogonal (**e**) visual space. Schematics above illustrate the relationship between spine and dendrite RFs for each bin. Spine numbers are indicated above bars. *P* values from permutation tests, $n = 44$ dendrites, 17 mice. **f**, Left, representative natural image. Green and purple squares represent co-axially and orthogonally displaced image sub-regions from a reference sub-region (red square). Local dominant orientation (Ori) of sub-regions is indicated below. Right, probability of co-occurrence of features with similar orientations (ΔOrientation <30°) in natural images for pairs of image features spatially displaced co-axially or orthogonally according to their orientation. The two distributions are significantly different for all displacements beyond 2° (2–50°, bin size of 2°, $P < 0.01$, Wilcoxon rank sum tests, Bonferroni correction for multiple comparisons).

postsynaptic neuron's orientation preference, but were as likely to prefer orthogonal orientations (Fig. 3c, e, $P = 0.7$). The structure, size and goodness of Gaussian fit of input RFs in co-axial and orthogonal visual space were similar as well as their distribution along the dendritic tree (see Methods, all P values >0.1, Kolmogorov–Smirnov tests). Thus neurons with displaced RFs preferentially connect if their RFs are co-oriented and aligned along the axis of their preferred orientation. This functionally specific connectivity between neurons processing different parts of visual space matches the statistics of edge co-occurrence in natural images, wherein edges of the same orientation occur more often along a common axis (Fig. 3f; see Methods)[18,25].

In this study we show that individual L2/3 pyramidal cells in mouse visual cortex receive diverse excitatory inputs encoding distinct visual features from an expansive area of the visual field. Inputs representing similar visual features from overlapping locations in visual space were more likely to terminate on nearby spines, consistent with the idea that co-active inputs cluster on dendritic branches[21,22]. Neighbouring inputs might cooperate to generate nonlinear dendritic events that contribute to a neuron's output[23,24]. On average, synaptic input was functionally biased for the stimulus orientation preferred by the postsynaptic neuron, consistent with previous work[7–10,20,21]. However, retinotopically displaced inputs provided specific contextual information, whereby neurons representing the same orientations preferentially connected if their RFs were separated along the axis of their preferred orientation. Our results are in keeping with predictions of studies in visual cortex of higher mammals, which revealed an anisotropic spread of axonal projections[13,15,16] and correlated firing of L5 and L6 neurons with overlapping RFs and matched orientation preference[26], but which could not determine the functional identity of inputs received by individual neurons.

Potential sources of input from regions of visual space outside a neuron's RF include lateral axonal connections within V1, as well as projections from the thalamus or feedback from higher visual areas[1,3,27]. Irrespective of the sources of retinotopically displaced inputs, the preferential connectivity between neurons with co-linearly aligned RFs may arise via activity-dependent mechanisms of synaptic plasticity driven by the exposure to extended contours in the visual environment. Indeed, the composition of retinotopically displaced inputs reflects the long-range image statistics of natural scenes, in which co-linearly aligned edges are enriched (Fig. 3f)[18,25]. Thus the patterns of synaptic connectivity may store the history of correlated firing of feature detectors in primary visual cortex[28].

Neurons with co-axially aligned and orientation-matched RFs would be co-activated by contours or edges extending in visual space, and may thus contribute to the facilitation of V1 responses by collinearly arranged line segments[17,29,30]. This specific organization of long-range connectivity, in combination with feedback from other cortical areas[4], provides a plausible circuit substrate for perceptual phenomena such as edge detection, visual contour integration and object grouping[17,18].

Online Content Methods, along with any additional Extended Data display items and Source Data, are available in the online version of the paper; references unique to these sections appear only in the online paper.

Received 24 November 2016; accepted 12 June 2017.
Published online 12 July 2017.

1. Rockland, K. S. & Lund, J. S. Intrinsic laminar lattice connections in primate visual cortex. *J. Comp. Neurol.* **216,** 303–318 (1983).
2. Gilbert, C. D. & Wiesel, T. N. Columnar specificity of intrinsic horizontal and corticocortical connections in cat visual cortex. *J. Neurosci.* **9,** 2432–2442 (1989).
3. Angelucci, A. & Bressloff, P. C. Contribution of feedforward, lateral and feedback connections to the classical receptive field center and extra-classical receptive field surround of primate V1 neurons. *Prog. Brain Res.* **154,** 93–120 (2006).
4. Gilbert, C. D. & Li, W. Top-down influences on visual processing. *Nat. Rev. Neurosci.* **14,** 350–363 (2013).
5. Yoshimura, Y., Dantzker, J. L. M. & Callaway, E. M. Excitatory cortical neurons form fine-scale functional networks. *Nature* **433,** 868–873 (2005).
6. Morgenstern, N. A., Bourg, J. & Petreanu, L. Multilaminar networks of cortical neurons integrate common inputs from sensory thalamus. *Nat. Neurosci.* **19,** 1034–1040 (2016).
7. Ko, H. *et al.* Functional specificity of local synaptic connections in neocortical networks. *Nature* **473,** 87–91 (2011).
8. Cossell, L. *et al.* Functional organization of excitatory synaptic strength in primary visual cortex. *Nature* **518,** 399–403 (2015).
9. Wertz, A. *et al.* Single-cell-initiated monosynaptic tracing reveals layer-specific cortical network modules. *Science* **349,** 70–74 (2015).
10. Lee, W.-C. A. *et al.* Anatomy and function of an excitatory network in the visual cortex. *Nature* **532,** 370–374 (2016).
11. Markov, N.T. *et al.* Weight consistency specifies regularities of macaque cortical networks. *Cereb Cortex* **21,** 1254–1272 (2011).
12. Malach, R., Amir, Y., Harel, M. & Grinvald, A. Relationship between intrinsic connections and functional architecture revealed by optical imaging and *in vivo* targeted biocytin injections in primate striate cortex. *Proc. Natl Acad. Sci. USA* **90,** 10469–10473 (1993).
13. Bosking, W. H., Zhang, Y., Schofield, B. & Fitzpatrick, D. Orientation selectivity and the arrangement of horizontal connections in tree shrew striate cortex. *J. Neurosci.* **17,** 2112–2127 (1997).
14. Martin, K. A. C., Roth, S. & Rusch, E. S. Superficial layer pyramidal cells communicate heterogeneously between multiple functional domains of cat primary visual cortex. *Nat. Commun.* **5,** 5252 (2014).
15. Sincich, L. C. & Blasdel, G. G. Oriented axon projections in primary visual cortex of the monkey. *J. Neurosci.* **21,** 4416–4426 (2001).
16. Schmidt, K. E., Goebel, R., Löwel, S. & Singer, W. The perceptual grouping criterion of colinearity is reflected by anisotropies of connections in the primary visual cortex. *Eur. J. Neurosci.* **9,** 1083–1089 (1997).
17. Kapadia, M. K., Ito, M., Gilbert, C. D. & Westheimer, G. Improvement in visual sensitivity by changes in local context: parallel studies in human observers and in V1 of alert monkeys. *Neuron* **15,** 843–856 (1995).
18. Geisler, W. S., Perry, J. S., Super, B. J. & Gallogly, D. P. Edge co-occurrence in natural images predicts contour grouping performance. *Vision Res.* **41,** 711–724 (2001).
19. Chen, X., Leischner, U., Rochefort, N. L., Nelken, I. & Konnerth, A. Functional mapping of single spines in cortical neurons *in vivo*. *Nature* **475,** 501–505 (2011).
20. Chen, T.-W. *et al.* Ultrasensitive fluorescent proteins for imaging neuronal activity. *Nature* **499,** 295–300 (2013).
21. Wilson, D. E., Whitney, D. E., Scholl, B. & Fitzpatrick, D. Orientation selectivity and the functional clustering of synaptic inputs in primary visual cortex. *Nat. Neurosci.* **19,** 1003–1009 (2016).
22. Takahashi, N. *et al.* Locally synchronized synaptic inputs. *Science* **335,** 353–356 (2012).
23. Smith, S. L., Smith, I. T., Branco, T. & Häusser, M. Dendritic spikes enhance stimulus selectivity in cortical neurons *in vivo*. *Nature* **503,** 115–120 (2013).
24. Stuart, G. J. & Spruston, N. Dendritic integration: 60 years of progress. *Nat. Neurosci.* **18,** 1713–1721 (2015).
25. Sigman, M., Cecchi, G. A., Gilbert, C. D. & Magnasco, M. O. On a common circle: natural scenes and Gestalt rules. *Proc. Natl Acad. Sci. USA* **98,** 1935–1940 (2001).
26. Schwarz, C. & Bolz, J. Functional specificity of a long-range horizontal connection in cat visual cortex: a cross-correlation study. *J. Neurosci.* **11,** 2995–3007 (1991).
27. Roth, M. M. *et al.* Thalamic nuclei convey diverse contextual information to layer 1 of visual cortex. *Nat. Neurosci.* **19,** 299–307 (2016).
28. Ko, H. *et al.* The emergence of functional microcircuits in visual cortex. *Nature* **496,** 96–100 (2013).
29. Nelson, J. I. & Frost, B. J. Intracortical facilitation among co-oriented, co-axially aligned simple cells in cat striate cortex. *Exp. Brain Res.* **61,** 54–61 (1985).
30. Chisum, H. J., Mooser, F. & Fitzpatrick, D. Emergent properties of layer 2/3 neurons reflect the collinear arrangement of horizontal connections in tree shrew visual cortex. *J. Neurosci.* **23,** 2947–2960 (2003).

Acknowledgements We thank T. Mrsic-Flogel, P. Znamenskiy, D. Muir as well as members of the Hofer and Mrsic-Flogel laboratories for insightful comments and suggestions and J. Dahmen and L. Cossell for analysis code and advice. We thank the GENIE Program and Janelia Farm Research Campus of the Howard Hughes Medical Institute for making GCaMP6 material available. This work was supported by the European Research Council (SBH), and the Biozentrum core funds.

Author Contributions M.F.I. and I.T.G. performed the experiments and analysed the data. All authors wrote the paper.

Author Information Reprints and permissions information is available at www.nature.com/reprints. The authors declare no competing financial interests. Readers are welcome to comment on the online version of the paper. Publisher's note: Springer Nature remains neutral with regard to jurisdictional claims in published maps and institutional affiliations. Correspondence and requests for materials should be addressed to S.B.H. (sonja.hofer@unibas.ch).

Reviewer Information *Nature* thanks K. Harris, M. Hubener and K. Svoboda for their contribution to the peer review of this work.

METHODS

Animals and surgical procedures. All experimental procedures were carried out in accordance with institutional animal welfare guidelines, and licensed by the Veterinary Office of the Canton of Basel, Switzerland. Experiments in this study were performed in 31 male and female C57BL/6 mice, aged 2–4 months (spine RF mapping: 21 mice; neural population RF mapping: 7 mice; somatic and dendritic RF mapping: 3 mice).

Prior to surgery, the animals were injected with dexamethasone (2 mg kg^{-1}), atropine (0.05–0.1 mg kg^{-1}) and analgesics (carprofen, 5 mg kg^{-1}). General anaesthesia was induced with a mixture of fentanyl (0.05 mg kg^{-1}), midazolam (5.0 mg kg^{-1}), and medetomidine (0.5 mg kg^{-1}). Viral injection and window implantation were performed as described previously[20,31]. In brief, a craniotomy was performed over right V1 and for spine imaging 90–120 nl of a mixture of highly diluted AAV9-CaMKII-Cre (1:20,000) and AAV2/1-Syn-Flex-GCaMP6s-WPRE or AAV2/1-CAG-Flex-mRuby2-2A-GCaMP6s-WPRE was injected using a glass pipette and a pressure injection system (Picospritzer III, Parker) to achieve sparse labelling of 5–10 pyramidal cells. For population imaging 90 nl of AAV2/1-Syn-Flex-GCaMP6s-WPRE mixed with AAV9-CaMKII-Cre (1:1,000) or AAV2/1-Syn-GCaMP6s-WPRE were injected instead. The skin was sutured shut after the injections. Two to four weeks after virus injection a 4-mm diameter craniotomy was made over right V1 and was sealed with a glass coverslip and cyanoacrylate glue (UltraGel, Pattex). A head plate was attached to the skull using dental cement (Heraeus Sulzer or C&B). Animals were given antibiotics and analgesics (enrofloxacin 5 mg kg^{-1}, buprenorphine 0.1 mg kg^{-1}) at the end of surgeries and repeatedly during recovery. Imaging started at least 4 days later.

Two-photon calcium imaging and visual stimulation. For imaging, mice were lightly anaesthetized with chlorprothixene (1 mg kg^{-1}) and isoflurane (0.4–0.8% in 1:1 mixture of N_2O and O_2). Atropine was given to slightly dilate the pupil and reduce mucus secretion. Eyes were covered with eye ointment (Maxitrol). The ointment was reduced to a thin layer during imaging on the eye contralateral to the imaged hemisphere to keep it moist. The ipsilateral eye remained covered. Rectal temperature was kept constant at 37 °C via a heating pad (DC Temperature Controller, FHC). The pupil position was monitored throughout each experiment.

Imaging was performed using a commercial resonance scanning two-photon microscope (B-Scope; Thorlabs) and a Mai Tai DeepSee laser (SpectraPhysics) at 930 nm with a 40× water-immersion objective (0.8 NA; Olympus). Images of 512 × 512 pixels with fields of view of approximately 30 × 30 μm (dendritic imaging) or approximately 450 × 450 μm (neuronal population imaging) or approximately 250 × 250 μm (soma and dendrite imaging) were acquired at a frame rate of 15 Hz using ScanImage 4.2 (ref. 32). For population imaging experiments and comparison of dendritic and somatic calcium signals, a piezo z-scanner (P-726.1CD, Physik Instrumente) was used to rapidly move the objective in the z axis and acquire 2 image planes simultaneously at 15 Hz frame rate, separated by 10–50 μm in depth. The power supply of the monitor backlight was controlled using a custom-built circuit[33] to present visual stimuli only in-between the scanning of two subsequent lines.

Visual stimuli were generated in MATLAB using Psychophysics Toolbox[34] and presented on a calibrated LCD monitor (60 Hz refresh rate) positioned 20 cm from the left eye at approximately 45° to the long axis of the animal, covering approximately 110 × 80° of visual space. At the beginning of each experiment, the appropriate retinotopic position in visual cortex was determined using small grating stimuli at 12 positions arranged in a 4 × 3 grid. The monitor was positioned such that the preferred retinotopic position of the imaged neurons was roughly centred on the screen.

Receptive field mapping stimuli consisted of black (<0.05 candela m^{-2}) and white (43 candela m^{-2}) squares of 8 × 8° on a grey background (23 candela m^{-2}). The squares were presented one at a time and in random order at one of 120 positions (12 × 10 matrix covering a total area of 96 × 80°; each position was repeated 12 times). The presentation rate was around 1.7 Hz and the duration of each stimulus was approximately 0.4 s, followed by 0.2 s blank screen. Sinusoidal gratings (0.03 cycles per degree, measured at the shortest distance between the eye and the monitor, 2 Hz, 100% contrast) drifting in 12 different directions for 1.5 s were presented randomly and were interleaved with a grey screen (around 2 s) between grating presentations. Each grating direction was repeated 10–12 times.

To measure visually evoked calcium signals in dendritic spines, individual neurons in layer 2/3 were selected for imaging based on several criteria: the baseline fluorescence of dendritic branches was high enough for dendritic spines to be visible, the nucleus was devoid of GCaMP6s expression, and cells exhibited selective visual responses and defined spatial receptive fields. After each recording, the focal plane and imaging position was checked and realigned with the initial image plane if necessary, and dendrites were carefully monitored for indications of photo damage. Z-stacks of individual cells and their dendritic arbors were acquired after dendritic imaging by averaging 20 frames per plane using 1-μm z-steps. Each animal was imaged repeatedly over the course of 4–5 weeks.

Data analysis. All analyses were performed in MATLAB (MathWorks). Image stacks were registered[35] to a 200-frame average to correct for xy motion. Spine, dendrite and single-cell soma regions of interest (ROIs) were drawn manually. For population imaging data, a semi-automated algorithm was used to detect cell outlines, which were subsequently confirmed by visual inspection. This algorithm was based on morphological measurements of cell intensity, size and shape. The cell-based ROIs were then eroded to reduce the influence of the neuropil signal around the cell bodies.

All pixels within each ROI were averaged to yield a time course. Calcium $\Delta F/F_0$ signals were obtained by using the median between the 10th and 70th percentile over the entire fluorescence distribution as F_0. The $\Delta F/F$ trace was high-pass filtered at a cut-off frequency of 0.02 Hz to remove slow fluctuations in the signal. Single spine calcium signals were isolated from global dendritic signals using a subtraction procedure described previously[20] (Extended Data Fig. 1). Dendritic signals were removed from spine signals by subtracting a scaled version of the dendritic shaft signal where the scaling factor equals the slope of a robust regression (MATLAB function robustfit.m). For verification, we repeated the main analyses after selecting only those spines that showed no trial-to-trial correlation with the dendritic shaft signal after dendritic signal subtraction (77% spines, correlation coefficient not significantly different to trial shuffled controls, $P > 0.01$, Wilcoxon rank sum test; Extended Data Fig. 9). Importantly, for spines with RFs displaced from that of the dendrite, we re-extracted RFs after removing the trials during which the dendrite was active (defined as those trials in which the activity of the dendrite exceeded the mean average activity of all stimulus positions plus three standard deviations). 96% of spines still showed significant RFs which were highly similar to those computed from all trials and results were not changed (Extended Data Fig. 9). A fast non-negative deconvolution was used to denoise the calcium signals[36]. We found no difference between data obtained from apical or basal dendrites, these were therefore combined for all subsequent analysis.

RF estimation. The ON and OFF subfields of spatial RFs were derived separately by analysing the responses to white and black stimulus patches, respectively. A response was defined as the mean denoised calcium signal in a window of three to five frames. Usually the first frame that reached significance over the 120 stimulus positions ($P < 0.05$, one-way ANOVA) was the first frame of the response window. In some cases the response window was optimized through visual inspection. A one-way ANOVA across the 120 stimulus positions was then calculated for the averaged response within the defined response window. ROIs that did not pass this test for either subfield were excluded from further analysis. Raw RFs represent the mean response at each of the 12 × 10 stimulus positions. The raw RF was interpolated at 1° resolution, z-scored and smoothed with an 11 × 11° square filter. We then calculated the amount of overlap between the ON and OFF RFs as

$$\text{overlap} = \frac{\text{ON} \cap \text{OFF}}{\text{ON} \cup \text{OFF}}$$

where ON and OFF are the regions of visual space covered by ON and OFF subfields, respectively, after thresholding at 2 standard deviations above the mean. In the rare cases in which more than one region remained after this step, all but the one containing the strongest average response were removed. Thresholding of RF subfields and removal of additional subfields was only used to quantify the RF size and the degree of RF overlap. For ROIs with overlap <0.6 we combined the two maps by scaling them according to the significance of each subfield and assigning positive values to the smoothed ON subfield and negative values to the smoothed OFF subfield. The combined smoothed RF was parameterized by fitting a two-dimensional Gabor function using the Levenberg–Marquardt algorithm. The Gabor function is described by

$$G(x', y') = A\exp\left(-\frac{x'^2}{2\sigma_x^2} - \frac{y'^2}{2\sigma_y^2}\right)\cos(2\pi f x' + \varphi)$$

where

$$x' = (x - c_x)\cos\theta - (y - c_y)\sin\theta$$

$$y' = (x - c_x)\sin\theta + (y - c_y)\cos\theta$$

These equations describe an underlying two-dimensional cosine grating parameterized by θ (orientation), f (spatial frequency) and φ (phase), which is enveloped by a two-dimensional Gaussian function parameterized by

A (amplitude), (c_x, c_x) (centre of the Gaussian) and σ_x and σ_y (standard deviations of the Gaussian perpendicular to and parallel to the axis of the grating, respectively). The quality of the Gabor fit was assessed evaluating the summed square of residuals (SSE, obtained from the fit.m function in MATLAB). Only ROIs with SSE $<6.5 \times 10^{-9}$ and a Pearson's correlation coefficient between the Gabor fit and the smoothed RF >0.4 were included for further analyses. The Gabor fits were used to compare the amount of subfield overlap between pairs of spines (Extended Data Fig. 3). In this case, ON subfields were defined as the region in which pixels of the Gabor fit were >20% of maximum absolute value, max(abs(Gabor fit)). Similarly, OFF subfields were defined as the region in which pixels of the Gabor fit were <20% of the negative of the maximum absolute value, −max(abs(Gabor fit)). The amount of overlap was defined as

$$\text{overlap} = \frac{|A \cap B|}{|A \cup B|}$$

where A and B are the regions of visual space covered by the spine A and spine B ON, OFF, or both subfields.

A pixel-to-pixel Pearson's correlation coefficient of smoothed RFs was used as a measure of RF similarity. The orientation of the RFs was obtained from the Gabor fits (variable θ from the Gabor function) and the distance between RFs was calculated from the centre between the ON and OFF subfields in the Gabor fit. Each spine RF separated by more than 30° from the dendrite RF was assigned to co-axial or orthogonal visual space according to the position of its RF centre relative to the position of the dendrite RF centre and orientation (Fig. 3a). The co-axial space was defined as the visual space up to 45° on either side of the axis extending along the orientation of the dendritic RF, running through the dendrite RF centre (also referred to as the collinear axis). Conversely, the orthogonal space was the remaining visual space, beyond 45° off the dendritic RF's collinear axis (see Fig. 3a). Receptive field structure and size were similar between RFs in co-axial and orthogonal space as measured by $\sigma_x \sigma_y$ of the RF Gabor fit and their ratio, the orientation of the RFs and the area and axis length of the subfields (all P values >0.1, Kolmogorov–Smirnov tests). Moreover, errors of the Gabor fits and the correlation between the Gabor fits and the raw RFs were similar (all P values >0.7) and calcium responses in the two populations of spines showed similarly few co-occurring dendritic events and similarly low correlation with the dendritic calcium signal ($P > 0.4$).

To examine the retinotopic organization of synaptic inputs onto V1 neurons (Extended Data Fig. 7), we combined spine data from all cells with known cell body position. We correlated the relative RF positions of spines (separately for elevation and azimuth) with the location of the spine ROI in cortical space relative to the cell body on a series of axes parallel to the cortical surface spanning 360° at 1° intervals. The direction with the highest correlation between relative RF positions and relative cortical position of all spines was taken as the direction of the retinotopic gradient for azimuth and elevation, respectively. For multiple comparisons, a Kruskal–Wallis test was followed by a Wilcoxon rank-sum test. Reported P values are Bonferroni-corrected. The same procedure was repeated after averaging the relative RF position and cortical position of all spines with significant RFs on each dendrite (Extended Data Fig. 7c).

Receptive field transformation. To combine the position and orientation of all spine RFs (relative to dendritic RFs) in a common coordinate framework (Fig. 3b, c), we rotated the dendritic RFs such that their orientation was vertical ($\theta = 0$) and then translated them such that their centres were aligned at the same position (Extended Data Fig. 8a). The parameters of this transformation were then used to transform the RFs of all spines to maintain the spatial relationship of their RF to that of their parent dendrite (Extended Data Fig. 8b)[8,37].

Grating responses. As a quality control for the RF fitting, the orientation preference of spine signals derived from the RF structure was compared to that inferred from drifting gratings (Extended Data Fig. 2). The de-noised calcium signal averaged over the stimulus period was taken as the response to each grating direction. Responses from different trials were averaged to obtain the orientation tuning curve. First, the preferred orientation (θ_{pref}) of the cell was determined as the stimulus that produced the strongest response. The orientation tuning curve was then fitted, with the sum of two Gaussians centred on θ_{pref} and $\theta_{pref} + \pi$, of different amplitudes A1 and A2, both with equal width σ (constrained to >15°), and a constant baseline B. The preferred direction was adjusted by the angle at which the fitted tuning curve attained its maximum. The preferred orientation was taken as the modulus of the preferred direction to 180°. The mean firing rates for the different stimulus directions were tested for differences by one-way ANOVA. Only spines or dendrites with $P < 0.01$ and R^2 for the orientation tuning curve fitting >0.7 were included for further analysis.

Population RFs. The same RF mapping protocol and analysis was repeated at the population level, with the exception that the median of the responses, instead of the mean, was used to estimate the ON and OFF RFs. The cortical distance between a pair of cells was defined as the Euclidean distance between the centre of mass of their cell bodies in the imaged plane. Because the size of the imaged field of view determines the distribution of cell pair distances in the sampled population, we estimated the likelihood of finding a RF distance as the probability of a given RF distance for the sample of the cell pairs within a given range of cell pair distances using 50-μm intervals (Extended Data Fig. 5).

Cell morphology. We used the Simple Neurite Tracer plugin from ImageJ to analyse the z-stacks of individual cells and trace the imaged dendrites back to the cell body. We measured the distance along the dendrite between spines and the cell body after smoothing the traced skeleton with a moving average window of 4 pixels. We determined the branch order of imaged dendritic segments based on the number of bifurcations from the cell body, together with changes in branch thickness or trajectory after a bifurcation. To study the relationship between physical distance and RF properties of spines, we measured the inter-spine anatomical distances along traced dendrites making the simplifying approximation that the dendritic segment is one-dimensional rather than a tube.

Analysis of natural images. A set of 375 black and white images from the BBC documentary *The Life of Mammals* (2002), depicting natural scenes such as landscapes, animals or humans, of 384 × 208 pixels in size, was used to analyse the co-occurrence of similarly oriented edges in natural scenes. Each image was divided into multiple sub-regions of 36 pixels, equivalent to 16° in our stimulus display settings, corresponding to roughly twice the average size of an ON and OFF subdomain (approximately 8°diameter). For each image sub-region we detected edges using the Prewitt method (function edge.m, MATLAB) and analysed the orientations of the detected edges performing a Hough transformation (using the function Hough.m, MATLAB). We defined the local orientation for that image sub-region as that with the highest variance in the Standard Hough Transform matrix of the image. A variance threshold of 3.5 was set to match the visual perception of edges in a subset of images. Image sub-regions were considered 'oriented' if the variance exceeded this threshold and 'non-oriented' otherwise. Varying the threshold did not change the results (data not shown). In relation to each image sub-region we then calculated the proportion of other image sub-regions with similar orientations (Δorientation < 30°) in the collinear axis of the sub-region's orientation and the axis orthogonal to it as a function of distance (Fig. 3f).

Statistics. All statistical tests used in the manuscript were non-parametric, with no assumptions concerning normality or equality of variances. Statistical significance of sample distributions of the difference in orientation preference between dendrites and spines were determined with a permutation test (Figs 2e, f, 3d, e and Extended Data Fig. 9a–c, h, i). Permutation tests do not assume normality of underlying distributions, nor need the observations be independent. We randomly permuted the preferred orientation of the spines, calculated the difference in orientation preference between dendrites and spines for this shuffled data set and computed the mean of the distribution. We repeated this procedure 10000 times to obtain a distribution of values, and calculated the fraction of values exceeding the actual value of the non-permuted data. For Fig. 2c, d, the randomization procedure involved randomly permuting the RF distance for spine–dendrite pairs and then calculating an F statistic for the shuffled dataset. This procedure was repeated 10,000 times in order to assess the percentage of repetitions that produce F values greater than those obtained for the non-permuted data. This percentage then provided an estimate of the P values associated with RF distance effects under the null hypothesis. This procedure preserves the number of data points in each bin, addressing the problem of having few data points for a given group.

For Fig. 1g and Extended Data Fig. 9d the inter-spine distance was binned and the mean spatial RF correlation for spine pairs within each bin was calculated independently for each dendrite. The permutation test was performed by randomly permuting the spatial RF correlations within the different dendrites. Only dendrites with more than six spines with significant RFs were included in this analysis. The same analysis was applied for the similarity in orientation preference instead of spatial RF correlation in Fig. 1h and Extended Data Fig. 9e. These analyses were performed on the level of dendrites rather than individual spines to provide very conservative statistics, to avoid potential overestimation of significance owing to the large number of spine pairs, and because of the combination of dependent and independent data. Pooling all data and performing the permutation test on individual spine pairs gave very similar results. Other statistical tests used are described in the main text or the figure legends. No statistical methods were used to predetermine sample size, but sample sizes are consistent with those generally employed in the field. The experiments were not randomized. The investigators were not blinded to allocation during experiments and outcome assessment.

Code and data availability. Data and custom code are available upon reasonable request.

31. Holtmaat, A. *et al.* Long-term, high-resolution imaging in the mouse neocortex through a chronic cranial window. *Nat. Protocols* **4,** 1128–1144 (2009).
32. Pologruto, T. A., Sabatini, B. L. & Svoboda, K. ScanImage: flexible software for operating laser scanning microscopes. *Biomed. Eng. Online* **2,** 13 (2003).
33. Leinweber, M. *et al.* Two-photon calcium imaging in mice navigating a virtual reality environment. *J. Vis. Exp.* **50885,** e50885 (2014).
34. Brainard, D. H. The psychophysics toolbox. *Spat. Vis.* **10,** 433–436 (1997).
35. Guizar-Sicairos, M., Thurman, S. T. & Fienup, J. R. Efficient subpixel image registration algorithms. *Opt. Lett.* **33,** 156–158 (2008).
36. Vogelstein, J. T. *et al.* Fast nonnegative deconvolution for spike train inference from population calcium imaging. *J. Neurophysiol.* **104,** 3691–3704 (2010).
37. Reid, R. C. & Alonso, J.-M. Specificity of monosynaptic connections from thalamus to visual cortex. *Nature* **378,** 281–284 (1995).

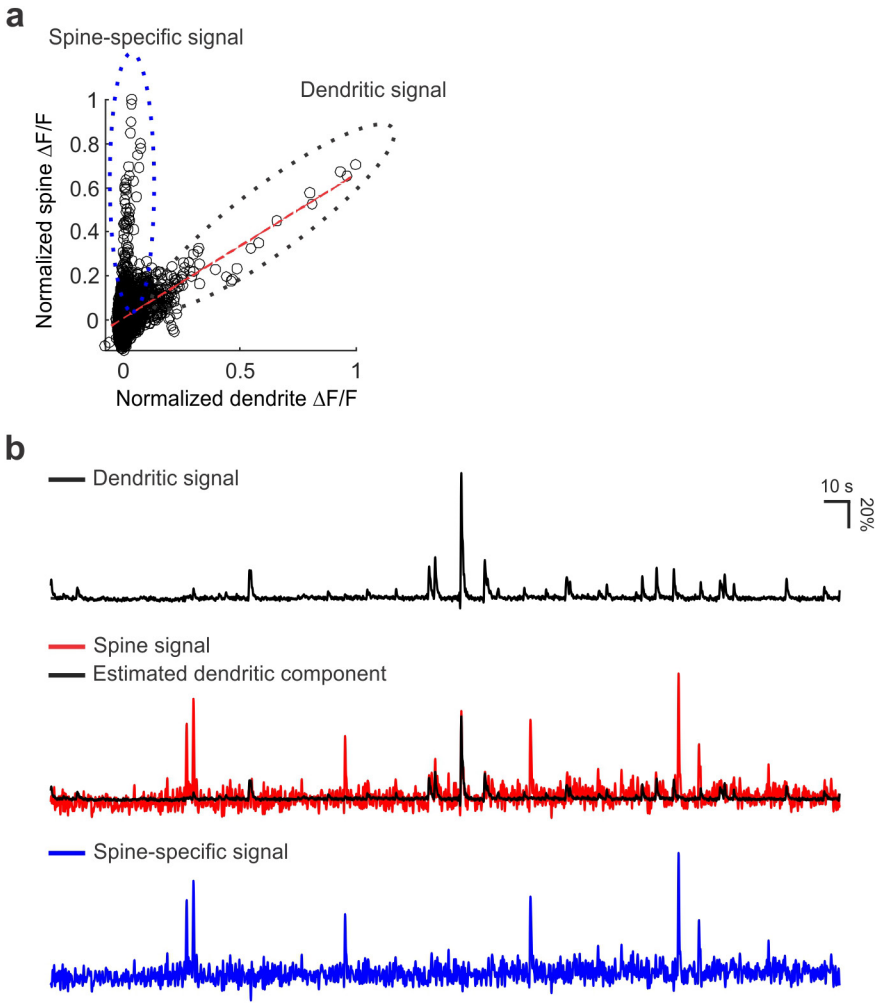

Extended Data Figure 1 | Isolation of spine-specific signals using robust regression. a, Calcium signal in the spine as a function of the signal in the corresponding dendritic shaft for one example spine. The slope of the robust fit (red dashed line), which indicates the contribution of dendritic activity to the spine signal, was used as a scaling factor. The scaled dendrite signal was then subtracted from the spine signal. **b**, Example traces of the calcium signal in the dendrite (top), the signal in the spine and the estimated dendritic component (scaled dendrite signal, middle) and the isolated spine-specific signal after subtraction (bottom).

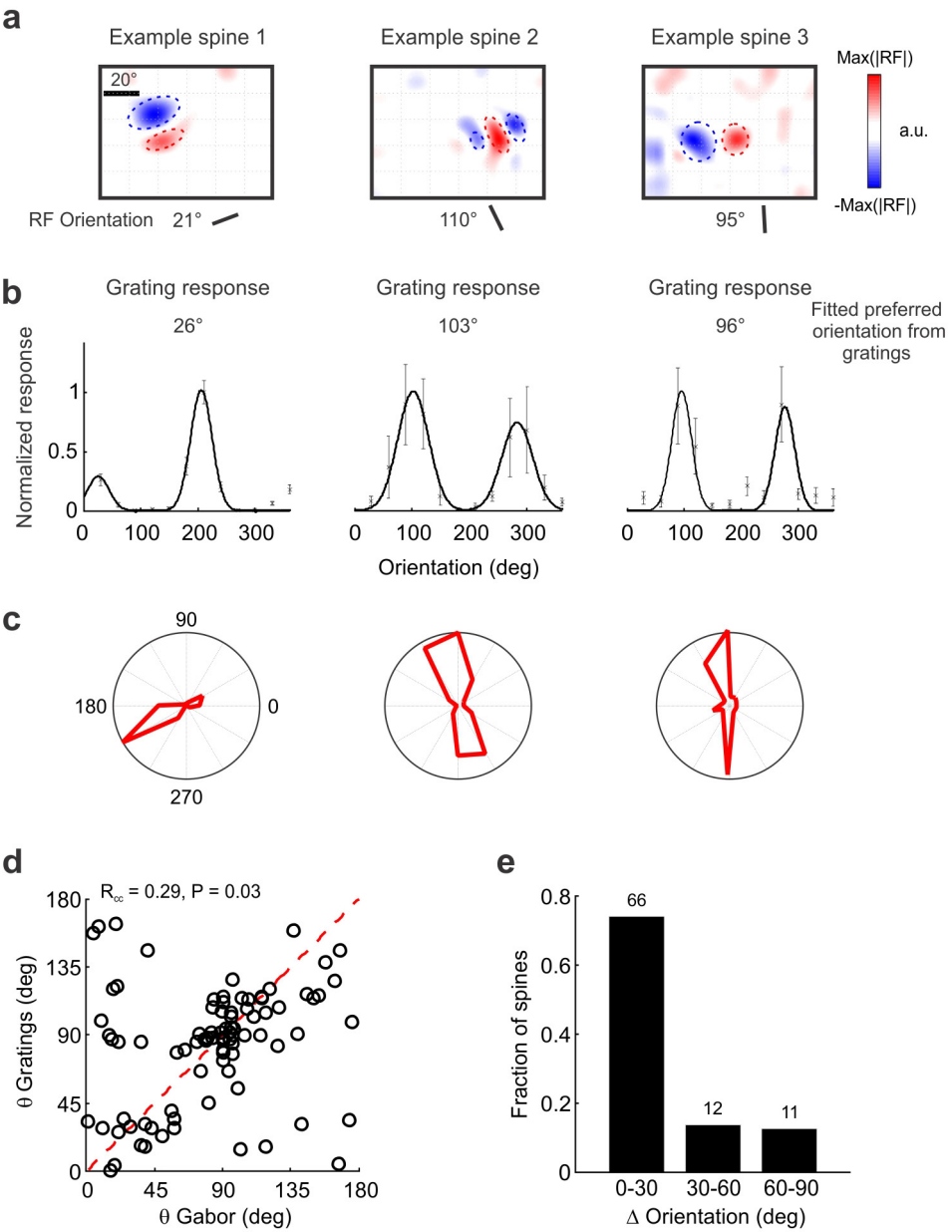

Extended Data Figure 2 | The relationship between orientation preference derived from spine RFs and drifting grating responses. **a**, Smoothed RFs (top), and orientation preference extracted from the RFs (bottom) for three example spines. a.u., arbitrary units. **b**, Example orientation tuning curves obtained using sinusoidal gratings for the same spines as in **a**. Normalized responses were fitted with the sum of two Gaussians (see Methods). Error bars indicate s.e.m. **c**, Polar plots of the grating responses above in **b**. **d**, Correspondence of orientation preference derived from responses to drifting gratings and from the RF Gabor fit of individual spines. Correlation coefficient and *P* value from circular correlation, $n = 89$ spines. **e**, The frequency of spines as a function of the difference in their orientation preference derived from RFs and grating responses (Δ Orientation). The majority of spines show similar orientation preferences for the two methods.

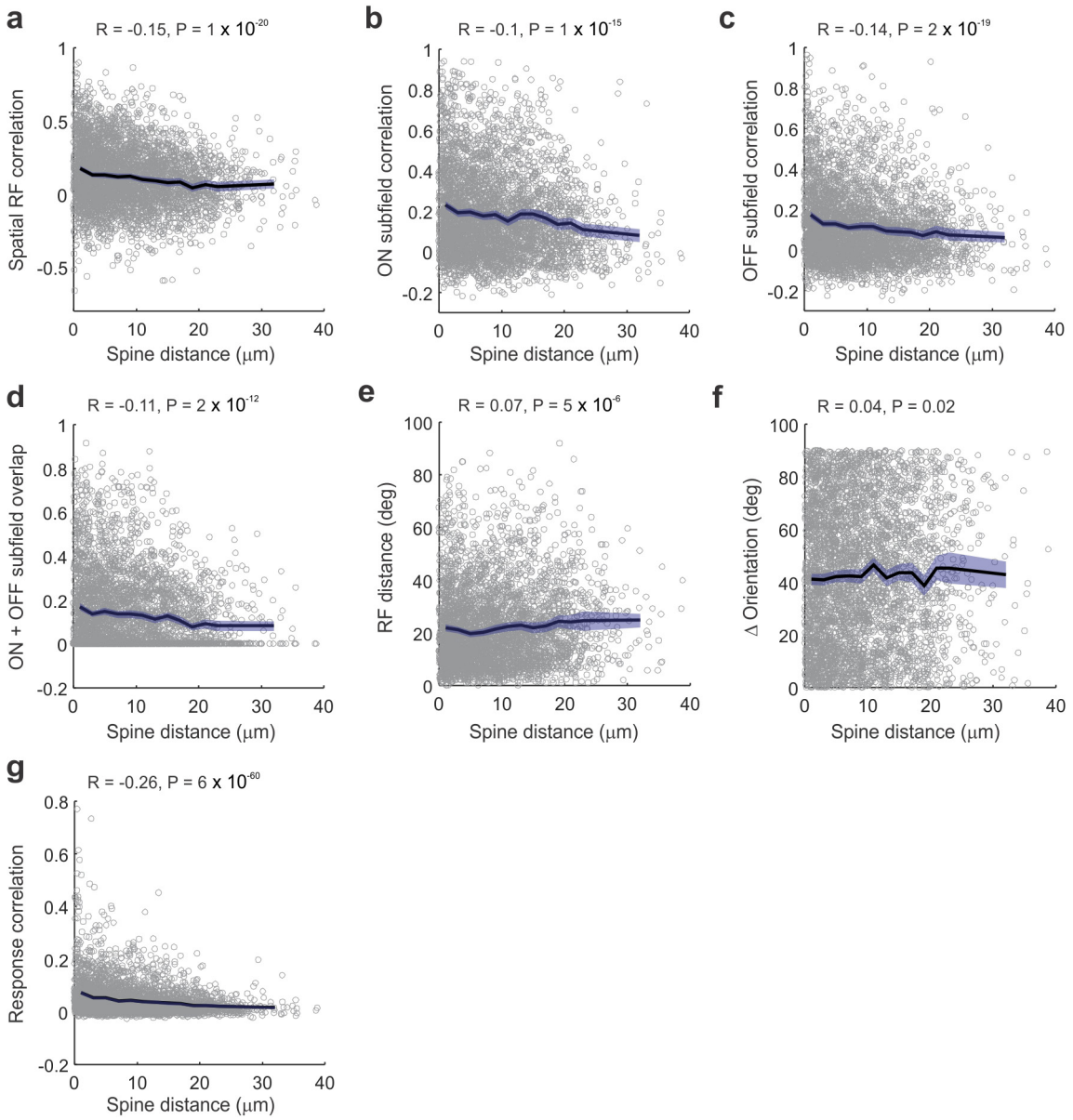

Extended Data Figure 3 | The relationship between spine pair distance and different visual response properties. a–g, Dendritic separation of spines pairs versus RF similarity (**a**, spatial RF correlation coefficients), ON subfield correlation coefficient (**b**), OFF subfield correlation coefficient (**c**), ON + OFF RF overlap (**d**, see Methods), RF centre distance (**e**), difference in orientation preference (**f**, Δ Orientation), and correlation coefficient of calcium signals (**g**, total correlation). $n = 3{,}966$ spine pairs, 74 dendrites, 21 mice. Blue shading represents the 95% confidence interval of the mean.

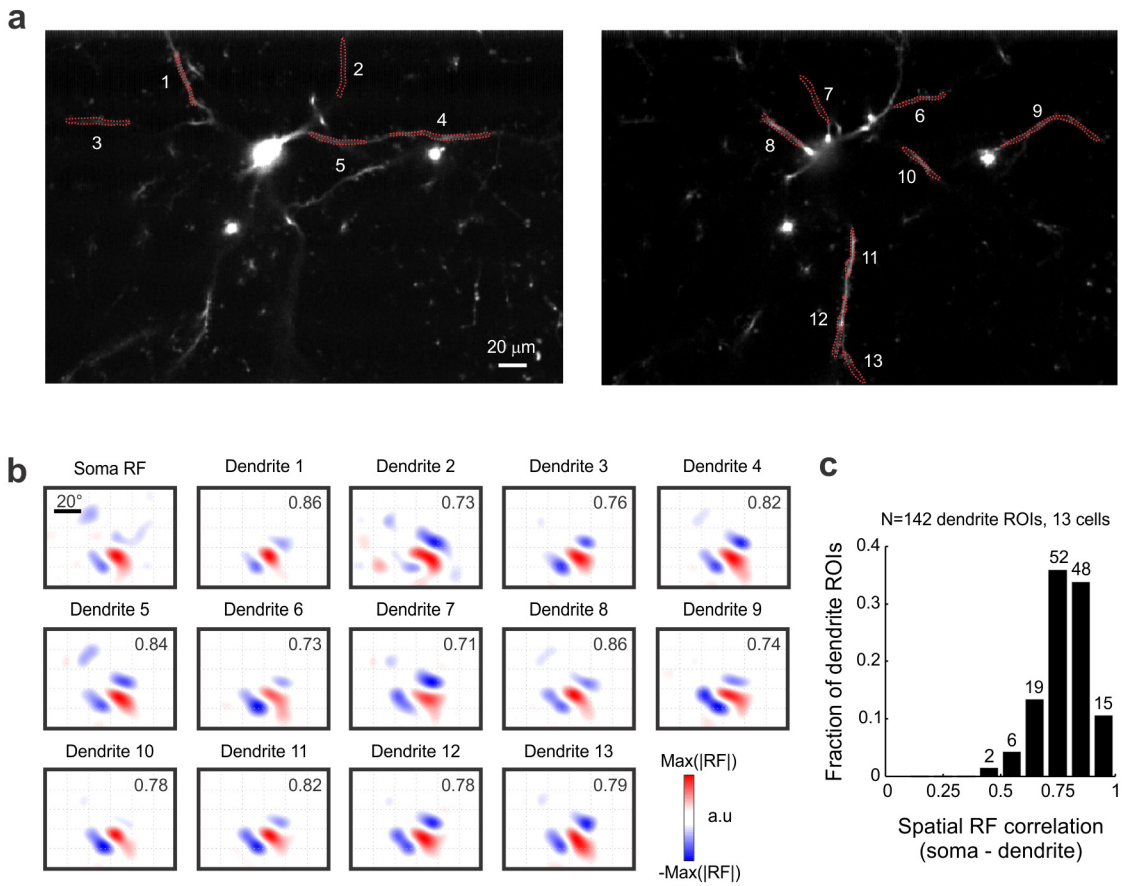

Extended Data Figure 4 | Simultaneous imaging of dendritic and somatic calcium signals. a, Two imaging planes separated by 10 μm comprising the soma and dendrites of a V1 layer 2/3 neuron expressing GCaMP6s. Dashed red lines indicate 13 dendritic ROIs from the same neuron. **b**, RFs calculated from calcium signals in the cell body and in the dendritic ROIs indicated in **a**. Numbers in the upper right corner of the dendritic RF maps indicate correlation with the somatic RF map. **c**, The frequency of dendrite ROIs as a function of the similarity of their RF with that of the soma (pixel-by-pixel RF map correlation). The majority of dendrites show similar RFs to that of the soma.

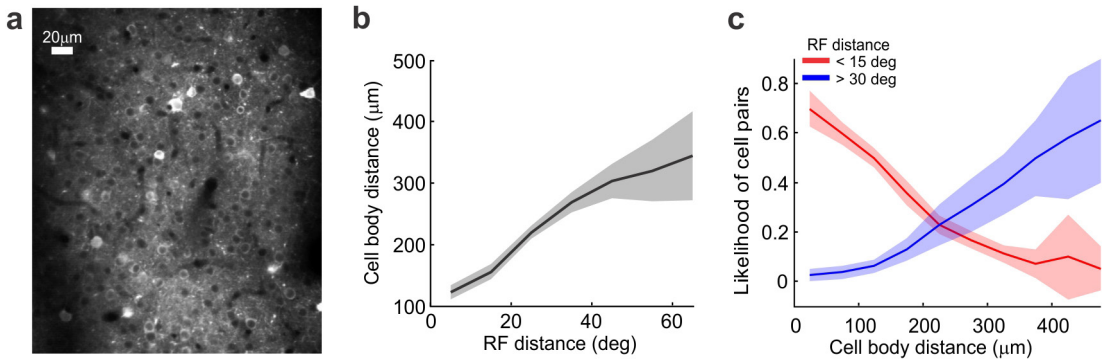

Extended Data Figure 5 | Relationship between the physical distance of somata and the distance of their RFs. a, Example imaging region with layer 2/3 neurons expressing GCaMP6s. **b**, Median physical cell body distance of all cell pairs as a function of the distance in visual space of their RFs. Shading indicates 95% confidence interval. **c**, Likelihood of encountering cell pairs with overlapping (<15° distance, red) and displaced (>30° distance, blue) RFs for different physical cell body distances.

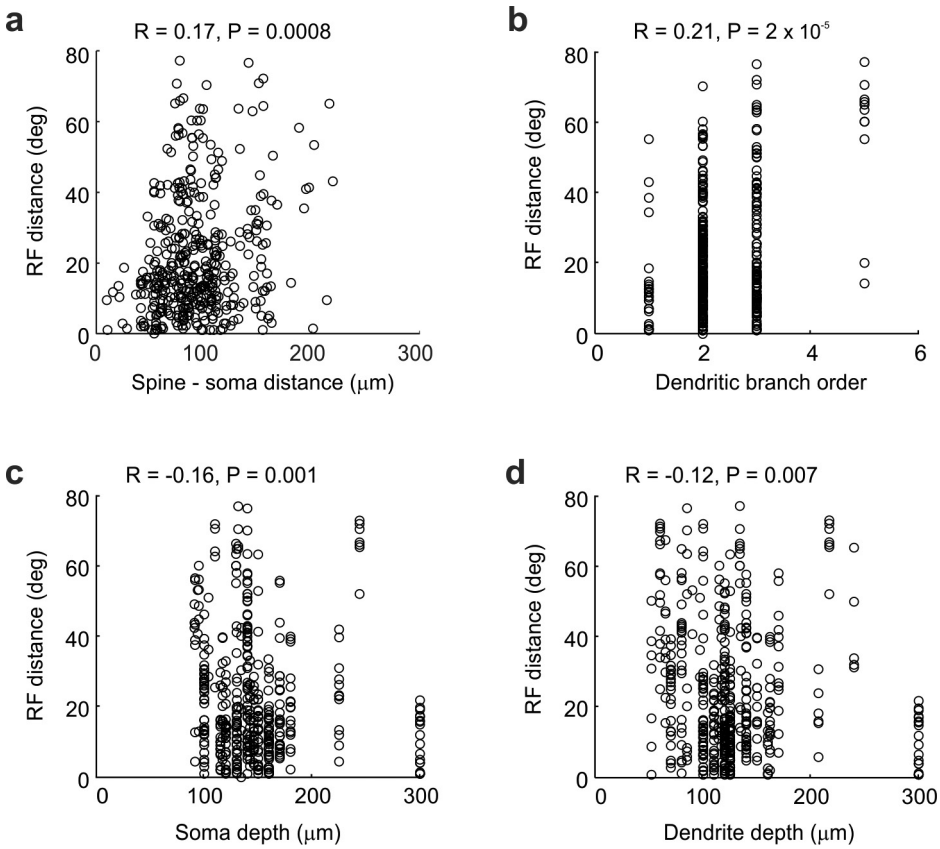

Extended Data Figure 6 | Anatomical location of spines with retinotopically displaced RFs. a–d, Distance in visual space of the RFs of spines from that of the parent neuron as a function of the physical distance between spine and soma measured along the dendritic tree (**a**), of the dendritic branch order of the dendrite (**b**), of the depth of the soma beneath the cortical surface (**c**), and of the depth of the imaged dendrite (**d**).

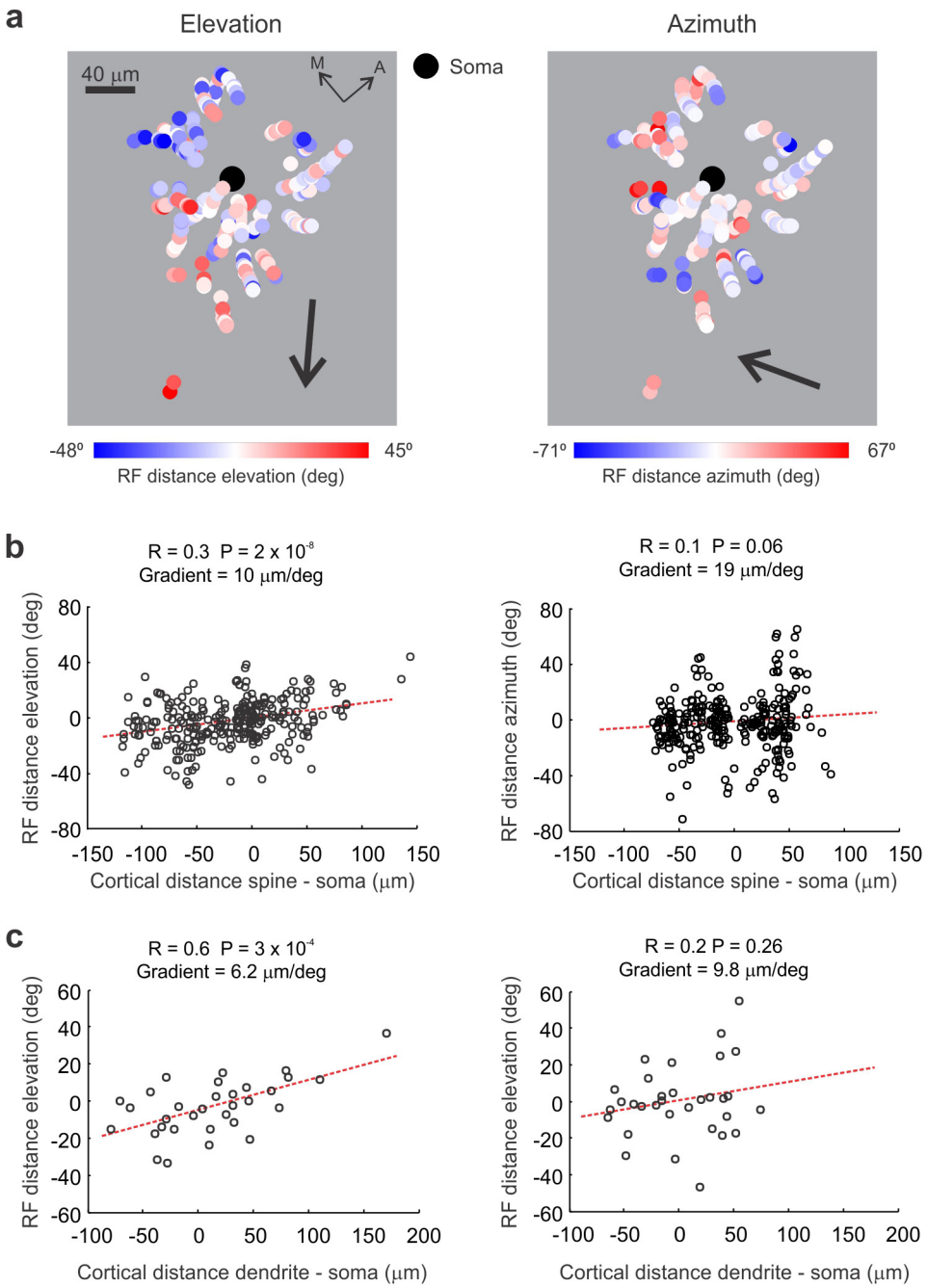

Extended Data Figure 7 | Retinotopic organization of visual inputs. **a**, Position of coloured dots indicates the cortical position of spines relative to the cell body on a plane parallel to the cortical surface. Dots are colour-coded according to the spines' RF position in visual field elevation (left) and visual field azimuth (right) relative to the parent neuron's RF. Spines from all cells are combined, aligned to the cell body position shown by the black dot. Arrows indicate axes of cortical space that correlate best with changes in receptive field elevation (left) or azimuth (right). **b**, Relationship between RF distance in elevation (left) and azimuth (right) and cortical distance of spines and soma in the direction of the best fit as indicated by arrows in **a**. **c**, Relationship between RF distance in elevation (left) and azimuth (right) and cortical distance of dendrites and soma in the direction of the best fit as indicated by arrows in **a**, after averaging the position and RF elevation or RF azimuth of all spines on the same dendritic branch. M, medial; A, anterior. $n = 32$ dendrites, 15 mice (all dendrites for which the cell body position was recovered).

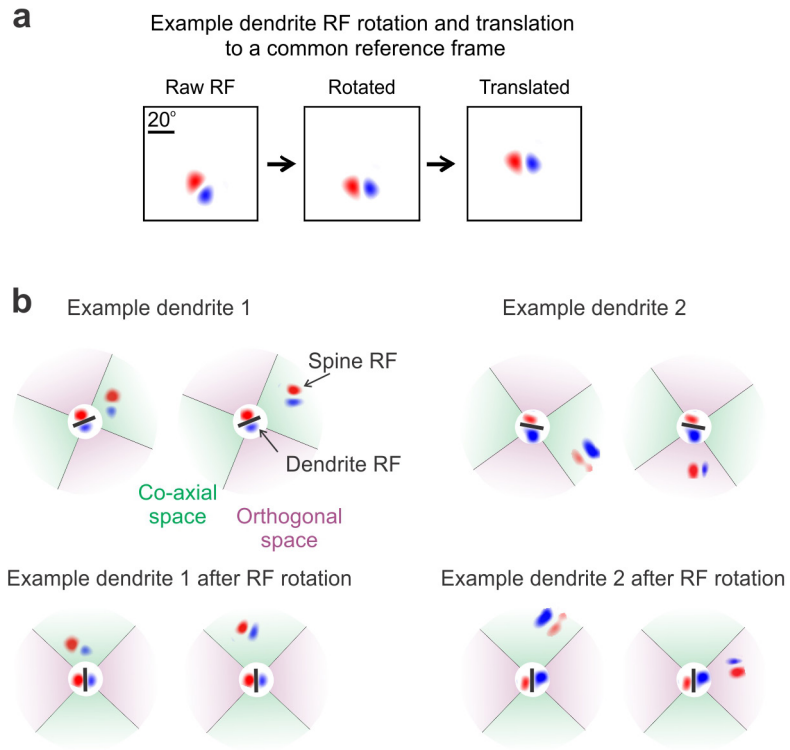

Extended Data Figure 8 | Transformation of dendrite and spine RFs. Transformation of RFs of dendrites and their corresponding spines for pooling of all spine RFs in Fig. 3b, c. **a**, To combine the position and orientation of all spine RFs relative to dendritic RFs in a common coordinate framework, we rotated the dendritic RFs such that their orientation was vertical and then translated them such that their centres were aligned at the same position. The parameters of this transformation were then used to transform the RFs of all spines to maintain the spatial relationship of their RF to that of their parent dendrite. **b**, RFs of two example dendrites and two of their corresponding spines before (top) and after transformation (bottom) as described in **a**. The visual space was defined as co-axial (green) or orthogonal (purple) relative to the centre and orientation of the dendrite RF.

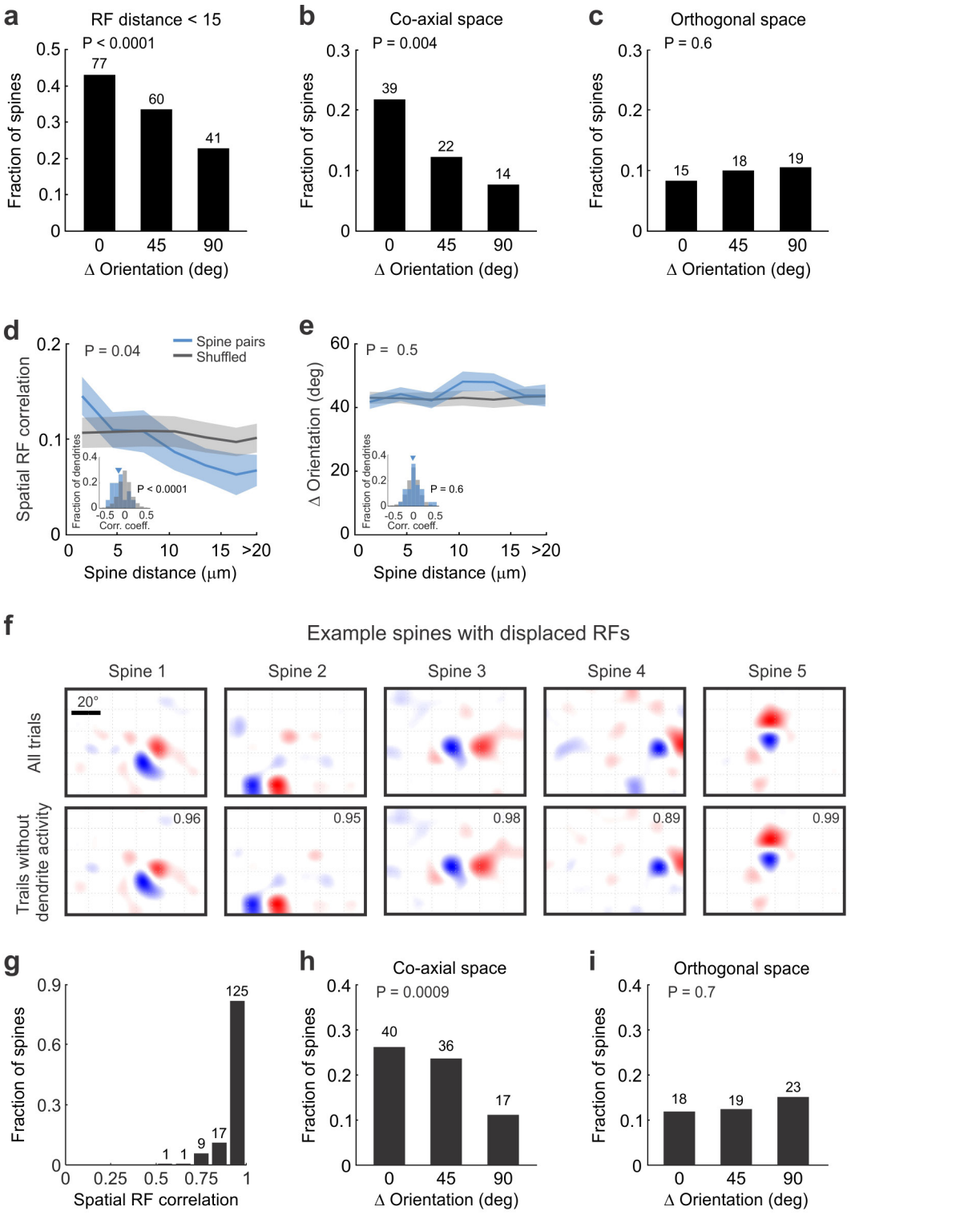

Extended Data Figure 9 | Control analysis for potential artefacts caused by global dendritic signals. a–e, Main analyses repeated after including only spines with responses not significantly correlated with the activity of their corresponding dendrite (see Methods, $n = 522$ spines, 26% of spines removed). **a**, Corresponds to Fig. 2e. **b**, Corresponds to Fig. 3d. **c**, Corresponds to Fig. 3e. **d**, Corresponds to Fig. 1g. **e**, Corresponds to Fig. 1h. **f–i**, Analyses of displaced spine RFs repeated after excluding all stimulus presentation trials in which the dendrite showed a calcium transient. **f**, Example RFs computed including all trials (top) or only trials in which the dendrite was not active (bottom). Numbers in the upper right corner indicate spatial RF correlation between the two RFs. **g**, Frequency of spines as a function of the similarity of their RF maps (spatial RF correlation) computed with and without trials with dendrite activity. **h**, Corresponds to Fig. 3d. **i**, Corresponds to Fig. 3e.